Materials Science & Engineering A 798 (2020) 140265

Contents lists available at ScienceDirect

Materials Science & Engineering A

journal homepage: http://www.elsevier.com/locate/msea

Crack initiation mechanism and fatigue life of titanium alloy Ti–6Al–2Sn–2Zr–3Mo-X: Effects of stress ratio and loading frequency

Chengqi Sun [a,b,*], Yanqing Li [c], Ruxu Huang [c], Lei Wang [c], Jialong Liu [d], Lingling Zhou [a], Guihua Duan [a]

[a] State Key Laboratory of Nonlinear Mechanics, Institute of Mechanics, Chinese Academy of Sciences, Beijing, 100190, China
[b] School of Engineering Science, University of Chinese Academy of Sciences, Beijing, 100049, China
[c] State Key Laboratory of Deep–sea Manned Vehicles (China Ship Scientific Research Center), Wuxi, 214082, China
[d] Institute of Geology and Geophysics, Chinese Academy of Sciences, Beijing, 100029, China

ARTICLE INFO

Keywords:
Ti–6Al–2Sn–2Zr–3Mo-X
Stress ratio
Frequency
Crack initiation mechanism
Fatigue life

ABSTRACT

In this paper, the fatigue behavior of Ti–6Al–2Sn–2Zr–3Mo-X alloy with basketweave microstructure is investigated at stress ratios $R = -1$, -0.5, 0.1 and 0.3 and loading frequencies $f = 0.4$ Hz, 4 Hz and 35 Hz. It is shown that the Ti–6Al–2Sn–2Zr–3Mo-X alloy presents two different crack initiation mechanisms. One is due to the cleavage of α grains and the other is due to the microstructure inhomogeneity and deformation incompatibility. For the former case, the fracture surface exhibits facet feature in the crack initiation region. For the latter case, the crack nucleates and initiates at α grains or interfaces and the fracture surface presents no facet feature in the crack initiation region. The higher stress ratio and the lower frequency tend to induce the higher probability for the occurrence of multiple crack initiation mode. Moreover, the paper indicates that the effect of stress ratio on fatigue life could be expressed as $N_f = A\,[(1–R)/2]^l \sigma^m_{a,R}$, where A, l and m are material parameters. The scatter of fatigue life is related to both the stress amplitude and the loading frequency. For relative higher stress amplitude, the fatigue life and the frequency at $R = -1$ could be correlated by a linear relation in log-log scale.

1. Introduction

The fatigue behavior of titanium alloys has drawn great attention due to their wide use in aerospace, marine engineering and so on [1–6]. Usually, the structural parts such as the blades of aero-engines and the pressure hulls of submersibles are subjected to fatigue loadings with different stress ratios or frequencies from the specimens tested in laboratory in service. Therefore, it is an important topic for the effects of stress ratio and loading frequency on the fatigue behavior of titanium alloys [7–11]. The results for Ti–15Mo–5Zr–3Al alloy indicated that the fatigue strength decreased with increasing the stress ratio ($R = -1$, 0, 0.5) and the crack initiation was related to the microstructure and stress ratio [12]. The high cycle fatigue strength in terms of maximum stress of α and β titanium alloys at $R = 0.1$ was shown much higher than that at $R = -1$, while the high cycle fatigue strength of $\alpha+\beta$ titanium alloys at $R = 0.1$ exhibited very small difference with that at $R = -1$ [13]. For Ti–6Al–4V alloys, three types of crack initiation (i.e. surface-without-facets, surface-with-facets and interior-with-facets) were observed in high cycle and very high cycle fatigue regimes [14]. It was shown that, with increasing the stress ratio ($R = -1$, -0.5, -0.1, 0.1, 0.5), the number of failed specimens decreased for surface-without-facets, increased for surface-with-facets, and increased first and then decreased for interior-with-facets. The fatigue strength decreased sharply for the failure types of surface-with-facets and interior-with-facets in very high cycle fatigue regime.

Regarding to the effect of loading frequency, it was indicated that the endurance limits for the titanium alloy VT23 [15] and the pseudo-α-titanium alloy [16] increased with increasing the loading frequency, in which the tested frequencies were 460 Hz, 3 kHz and 10 kHz for the titanium alloy VT23, and 30 Hz, 300 Hz and 10 kHz for the pseudo-α-titanium alloy. However, the ultrasonic frequency fatigue test (20 kHz) was shown no influence on the fatigue strength or fatigue life for Ti–6Al–4V alloy [17] and TC-17 alloy [18] in comparison with the conventional frequency fatigue test. Some other results of Ti–6Al–4V alloy at three heats (Heats A, B and C) indicated that the frequency effect ($f = 120$ Hz, 600 Hz, 20 kHz) was negligible for Heats A and B developing interior fractures, while the high frequency showed a higher fatigue strength for Heat C developing only surface fractures [19]. The

* Corresponding author. State Key Laboratory of Nonlinear Mechanics, Institute of Mechanics, Chinese Academy of Sciences, Beijing, 100190, China.
E-mail address: scq@lnm.imech.ac.cn (C. Sun).

https://doi.org/10.1016/j.msea.2020.140265
Received 12 June 2020; Received in revised form 1 August 2020; Accepted 8 September 2020
Available online 10 September 2020
0921-5093/© 2020 Elsevier B.V. All rights reserved.

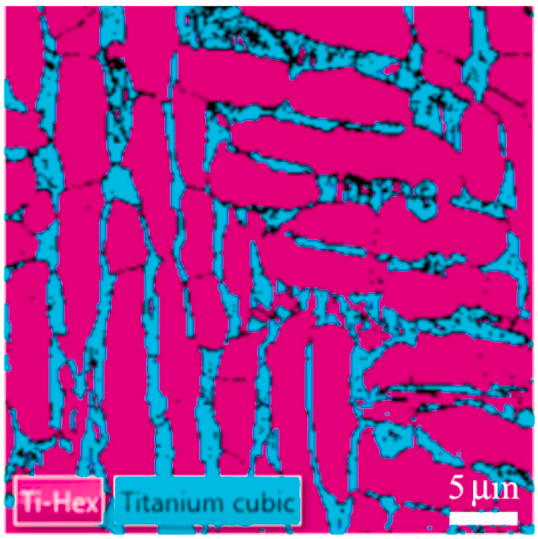

Fig. 1. EBSD picture of microstructure for the present Ti–6Al–2Sn–2Zr–3Mo-X alloy.

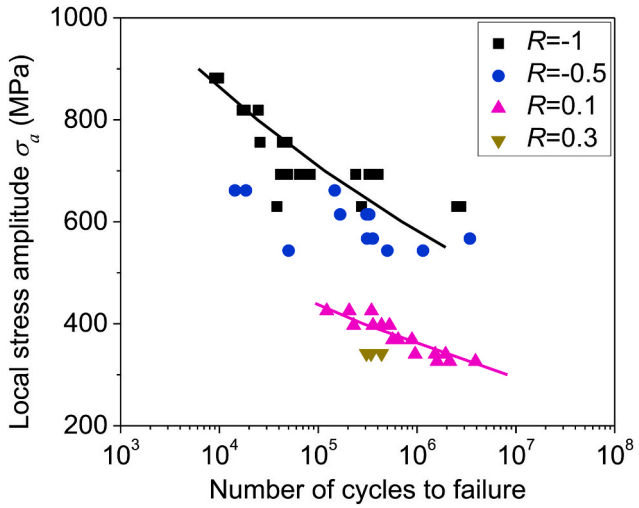

Fig. 2. Local stress amplitude versus fatigue life at different stress ratios, in which the lines denote the linear regression results of the fatigue life with the local stress amplitude in log-log scale.

frequency effect (f = 70 Hz, 400 Hz, 1800 Hz) was also shown to be related to the stress ratio for high cycle fatigue of Ti–6Al–4V alloy [20]. At low stress ratio, the fatigue strength increased with the increase of frequency.

The existing results indicate that the types of titanium alloy and their microstructures play important role in the effects of stress ratio and loading frequency on fatigue behavior. Ti–6Al–2Sn–2Zr–3Mo-X is a high strength titanium alloy with high fracture toughness, which has potential applications in structural components of marine engineering such as the pressure hulls of deep-sea submersibles and might subject to fatigue loadings in service. In this paper, axial loading fatigue tests are performed on Ti–6Al–2Sn–2Zr–3Mo-X with basketweave microstructure at different stress ratios ($R = -1$, −0.5, 0.1, 0.3) and loading frequencies (f = 0.4 Hz, 4 Hz, 35 Hz), and the effects of stress ratio and loading frequency on crack initiation mechanism and fatigue life of Ti–6Al–2Sn–2Zr–3Mo-X are investigated. It is observed that the crack initiation regions could exhibit facet feature or no facet feature at the tested stress ratios and frequencies. Then, the cross-section samples parallel to the loading direction are further prepared for the crack initiation regions by focused ion beam (FIB) technique and the mechanism of crack initiation are investigated by the scanning electron microscope (SEM) and electron backscatter diffraction (EBSD) observations. The effects of stress ratio and loading frequency on the fatigue life are also modeled and discussed.

2. Materials and methods

2.1. Materials

The material used is a high strength titanium alloy Ti–6Al–2Sn–2Zr–3Mo-X cut out from a forged flat plate parallel to the rolling direction. The tensile strength is 1072 MPa and the yield strength is 978 MPa. The microstructure of the material is basketweave consisting of α phase lamella and β_{trans}, as shown in Fig. 1.

2.2. Fatigue tests

The fatigue test is conducted on a servohydraulic test system at room temperature in air. Four stress ratios $R = -1$, −0.5, 0.1 and 0.3 are tested at the frequency $f = 35$ Hz, and three frequencies $f = 35$ Hz, 4 Hz and 0.4 Hz are performed at the stress ratio $R = -1$. The hourglass specimen with the minimum diameter of 5 mm is used [11]. The diameter of the parallel segment is 10 mm, and the total length of the specimen is 100 mm. The elastic stress concentration factor is 1.05, which is defined as the ratio of the maximum principal stress at the notch root to that of the smooth specimen with the same minimum diameter under the identical axial loading. The surface of the hourglass part of the specimen is ground and polished before fatigue test.

2.3. Observation methods

The fracture surfaces of failed specimens are observed by SEM. Moreover, several cross-section samples parallel to the loading direction are prepared for typical crack initiation regions by FIB technique on commercial crossbeam 540 FIB-SEM systems and then observed by SEM and EBSD on Nordlys of Oxford Instruments. The fracture surfaces of the cross-section samples are protected by a thin coating layer of platinum during the cutting process by FIB technique.

3. Results and discussions

3.1. Effect of stress ratio on fatigue life and crack initiation

3.1.1. Fatigue life

Fig. 2 shows the S–N data of the specimens at different stress ratios. The detailed information of the experimental results are listed in Tables 1 and 2, in which the fatigue life data at $R = -1$ is also shown in Ref. [11]. It is seen from Fig. 2 that the stress ratio has a significant influence on the fatigue life. With the increase of the stress ratio, the fatigue life decreases for the same local stress amplitude (the stress amplitude at the minimum cross section incorporating the elastic stress concentration factor 1.05).

Here, the effect of stress ratio on fatigue life is modeled. According to the work in Refs. [21,22], the effect of stress ratio on fatigue strength of some metallic materials (e.g. steels, aluminium alloys, magnesium alloys) in low cycle and high cycle fatigue regimes could be expressed as $\sigma_{a,R} = [(1\text{-}R)/2]^l$, where $\sigma_{a,R}$ denotes stress amplitude at stress ratio R, l is material parameter. Considering that the S–N curve is usually taken as the form of $N_f = A\sigma^m$, where N_f denotes fatigue life, σ is stress amplitude or maximum stress, A and m are material parameters, it is assumed that the fatigue life, stress amplitude and the stress ratio could be expressed as:

$$N_f = A\left(\frac{1-R}{2}\right)^l \sigma_{a,R}^m \quad (1)$$

Table 1
Experimental results of specimens at $R = -1$ and -0.5 shown in Fig. 2.

R = −1, f = 35 Hz				R = −0.5, f = 35 Hz			
σ_a (MPa)	N_f	Origin location	Single or Multi-site	σ_a (MPa)	N_f	Origin location	Single or Multi-site
882	8.98×10^3	Surface	Single	661.5	1.44×10^4	Surface	Single
882	9.40×10^3	Surface	Single	661.5	1.86×10^4	Surface	Single
882	9.82×10^3	Surface	Single	661.5	1.47×10^5	Surface	Single
819	1.79×10^4	Surface	Single	614.25	1.67×10^5	Surface	Single
819	2.48×10^4	Surface	Single	614.25	3.08×10^5	Surface	Single
819	1.82×10^4	Surface	Single	614.25	3.28×10^5	Surface	Single
819	1.70×10^4	Surface	Single	567	3.13×10^5	Surface	Multi
756	4.34×10^4	Surface	Single	567	3.56×10^5	Surface	Single
756	4.36×10^4	Surface	Single	567	3.42×10^6	Surface	Single
756	2.58×10^4	Surface	Single	543.375	5.0×10^5	Surface	Single
756	4.83×10^4	Surface	Single	543.375	5.02×10^4	Surface	Single
693	2.39×10^5	Surface	Single	543.375	1.15×10^6	Surface	Single
693	6.45×10^4	Surface	Single				
693	3.27×10^5	Surface	Single				
693	7.97×10^4	Surface	Single				
693	4.04×10^5	Surface	Single				
693	4.16×10^4	Surface	Single				
693	4.90×10^4	Surface	Single				
693	8.29×10^4	Surface	Single				
630	2.74×10^5	Surface	Single				
630	2.77×10^6	Surface	Single				
630	2.52×10^6	Interior	Single				
630	3.82×10^4	Surface	Single				

Table 2
Experimental results of specimens at $R = 0.1$ and 0.3 shown in Fig. 2.

$R = 0.1, f = 35$ Hz				$R = 0.3, f = 35$ Hz			
σ_a (MPa)	N_f	Origin location	Single or Multi-site	σ_a (MPa)	N_f	Origin location	Single or Multi-site
425.25	3.46×10^5	Surface	Single	341.775	3.07×10^5	Interior	Single
425.25	2.06×10^5	Surface	Multi	341.775	4.37×10^5	Surface	Multi
425.25	1.22×10^5	Surface	Single	341.775	3.43×10^5	Interior	Single
396.9	5.26×10^5	Surface Interior	Multi				
396.9	3.58×10^5	Surface	Single				
396.9	2.28×10^5	Surface	Single				
396.9	4.37×10^5	Surface	Single				
368.55	5.66×10^5	Surface	Single				
368.55	6.44×10^5	Surface	Single				
368.55	8.89×10^5	Surface	Single				
340.2	9.55×10^5	Surface	Single				
340.2	1.94×10^6	Surface	Single				
340.2	1.53×10^6	Interior	Single				
326.025	1.60×10^6	Surface	Single				
326.025	3.90×10^6	Surface	Single				
326.025	2.14×10^6	Surface	Single				

Firstly, the parameters A and m are determined as $A = 10^{38.332}$ and $m = -11.693$ by the linear regression for the fatigue life data with the local stress amplitude in log-log scale at the stress ratio $R = -1$. The linear regression curve is shown in Fig. 2.

Substitution of the values of A and m into Eq. (1), we have

$$N_f = 10^{38.332}\left(\frac{1-R}{2}\right)^{l}\sigma_{a,R}^{-11.693} \tag{2}$$

Then, the linear regression analysis is performed for the fatigue life data with the local stress amplitude in log-log scale at the stress ratio $R = 0.1$ by assuming the same value of m as that obtained at the stress ratio $R = -1$, i.e.

$$N_f = 10^{35.879}\sigma_{a,0.1}^{-11.693} \tag{3}$$

The linear regression result for the fatigue life data with the local stress amplitude at the stress ratio $R = 0.1$ is also shown in Fig. 2.

From Eqs. (2) and (3), we have $l = 7.073$.

Finally, substitution of $l = 7.073$ into Eq. (2), the formula for the fatigue life, stress amplitude and the stress ratio is obtained as

$$N_f = 10^{38.332}\left(\frac{1-R}{2}\right)^{7.073}\sigma_{a,R}^{-11.693} \tag{4}$$

From Eq. (4), for the same fatigue life, the stress amplitudes at the stress ratios R_1 and R_2 satisfy

$$\frac{\sigma_{a,R_1}}{\sigma_{a,R_2}} = \left(\frac{1-R_2}{1-R_1}\right)^{-0.605} \tag{5}$$

Especially, we have

$$\sigma_{a,R} = \sigma_{a,-1}\left(\frac{1-R}{2}\right)^{0.605} \tag{6}$$

Fig. 3 shows the predicted median S–N curves (i.e. 50% survival probability curves) at the stress ratios $R = -0.5$, 0.1 and 0.3 by using the median S–N curve at the stress ratio $R = -1$. For the median S–N curve at $R = -1$, it is obtained as that in literature [6,23] for the fatigue life data at different stress amplitudes, in which the fatigue life in logarithm of base 10 is assumed to follow the two parameter Weibull distribution. It is seen that the predicted median S–N curves at the stress ratios $R =$

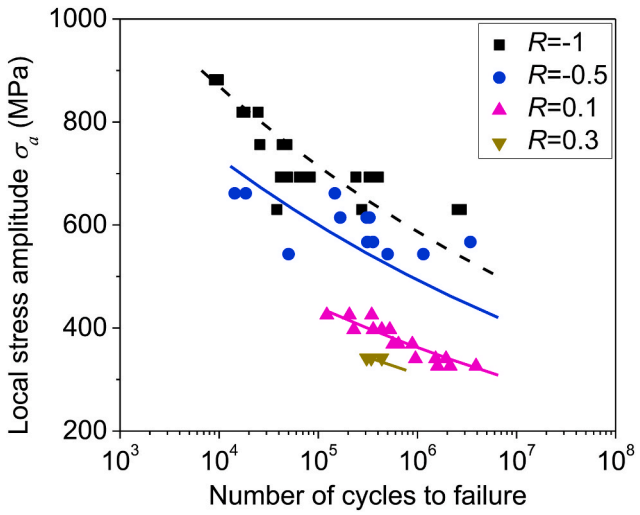

Fig. 3. Comparison of predicted median S–N curves with experimental data, in which the dashed line denotes the predicted result by the experimental data at the stress ratio $R = -1$, and the solid lines denote the predicted results by the median S–N curve at $R = -1$.

−0.5, 0.1 and 0.3 are generally in the middle of the experimental data, indicating that Eq. (1) correlates well the effect of stress ratio on the fatigue life of the present Ti–6Al–2Sn–2Zr–3Mo-X alloy.

3.1.2. Fracture surface observation

SEM observation indicates that the specimens tested at the stress ratio $R = -1$ fail from the specimen surface (Figs. 4a–d) except one specimen fails from the interior of the specimen (Fig. 4e and f) [11]. Moreover, it is observed that there is facet feature in the crack initiation region for individual specimen (Fig. 4d), similar to that observed in Ti-6246 alloy and Ti–6Al–4V [14,24,25].

The specimens tested at the stress ratio $R = -0.5$ all fail from the specimen surface, and one specimen presents multiple crack initiation sites (Fig. 5a–c). The facet feature is also found in the crack initiation region of individual specimen at the stress ratio $R = -0.5$ (Fig. 5e).

Most of the tested specimens at the stress ratio $R = 0.1$ fail from the specimen surface and a few fail from the specimen interior (Fig. 6c and e). Two specimens exhibit multiple crack initiation sites (Fig. 6c–e). Several specimens present facet feature in the crack initiation region at the stress ratio $R = 0.1$ (Fig. 6b).

For the specimens tested at the stress ratio $R = 0.3$, the surface crack initiation and the interior crack initiation are both observed at the fracture surface (Fig. 7). The multiple crack initiation sites (Fig. 7a–c) and the facet feature are also found in the crack initiation region

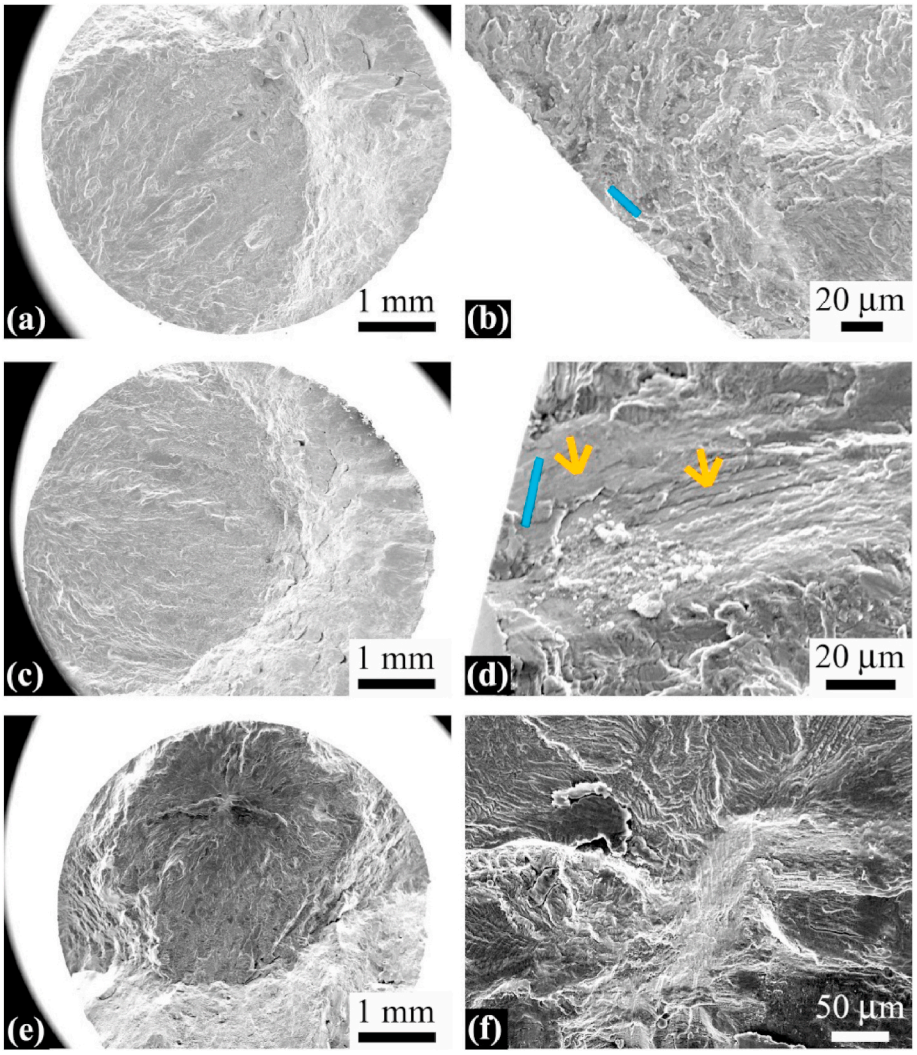

Fig. 4. Fracture surface morphology of failed specimens at the stress ratio $R = -1$. (a) and (b): $\sigma_{max} = 693$ MPa, $N_f = 6.45 \times 10^4$; (c) and (d): $\sigma_{max} = 693$ MPa, $N_f = 3.27 \times 10^5$; (e) and (f): $\sigma_{max} = 630$ MPa, $N_f = 2.52 \times 10^6$. (a), (c) and (e): Low magnification image of the fracture surface; (b), (d) and (f) Close-ups of crack initiation regions in (a), (c) and (e), respectively. The lines in (b) and (d) denote the locations prepared for the cross-section samples parallel to the loading direction. The arrows in (d) point to the regions exhibiting the facet feature.

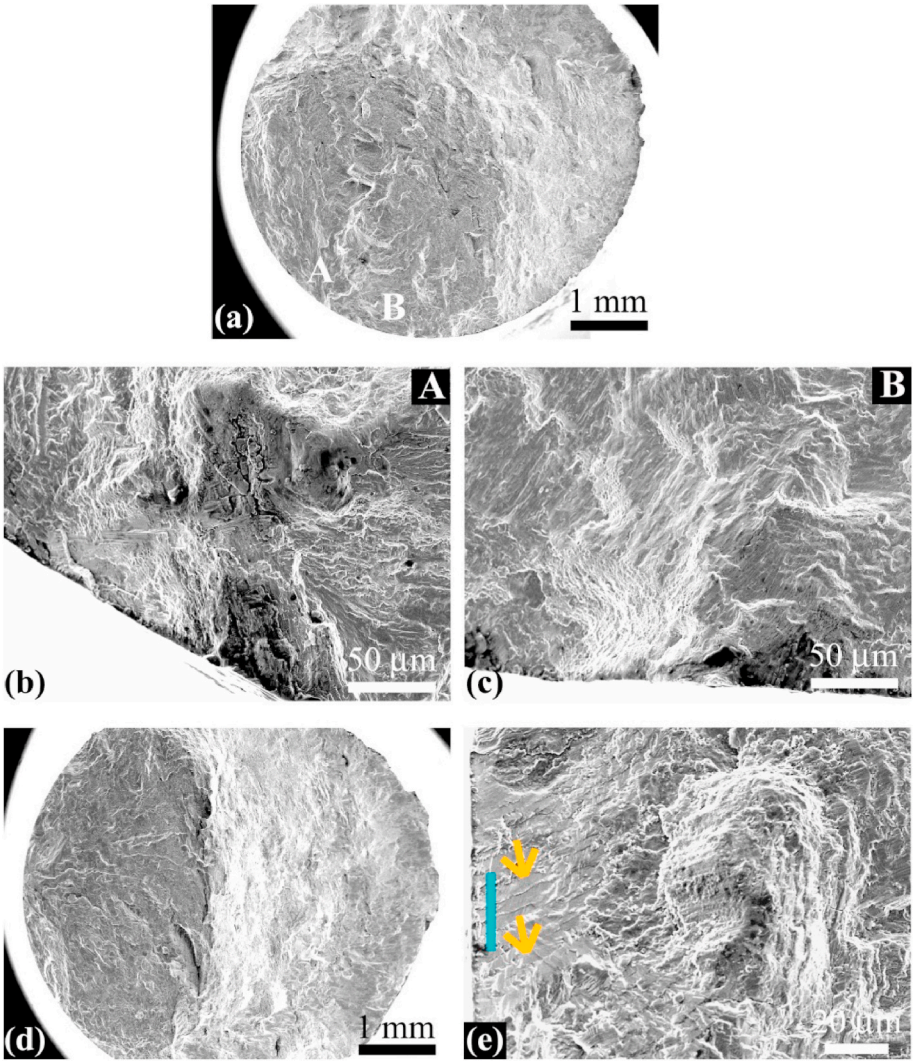

Fig. 5. Fracture surface morphology of failed specimens at the stress ratio $R = -0.5$. (a)–(c): Multiple crack initiation at $\sigma_{max} = 756$ MPa and $N_f = 3.13 \times 10^5$; (d) and (e): Single crack initiation at $\sigma_{max} = 819$ MPa and $N_f = 3.08 \times 10^5$. (a) and (d): Low magnification image of the fracture surface; (b) and (c) Close-ups of crack initiation regions at A and B in (a), respectively; (e) Close-up of crack initiation region in (d). The line in (e) denotes the location prepared for the cross-section sample parallel to the loading direction. The arrows in (e) point to the regions exhibiting the facet feature.

(Fig. 7c) at the stress ratio $R = 0.3$.

SEM observation indicates that the facet feature could present in the crack initiation region for all the tested stress ratios $R = -1$, -0.5, 0.1 and 0.3. For stress ratios $R = -0.5$, 0.1 and 0.3, both the single and multiple crack initiation modes are observed. While for the stress ratio $R = -1$, the tested specimens just present the single crack initiation mode. It seems that the stress ratio has influence on the crack initiation mode and the relative higher stress ratio has the higher probability for the occurrence of multiple crack initiation. For stress ratios $R = -1$, 0.1 and 0.3, both the surface and the interior crack initiation modes are observed. While the interior crack initiation is not observed at $R = -0.5$. So, it is thought that the stress ratio has no influence on the occurrence of surface crack initiation or interior crack initiation for the present Ti–6Al–2Sn–2Zr–3Mo-X alloy.

3.2. Effect of loading frequency on fatigue life and crack initiation

3.2.1. Fatigue life

Fig. 8 shows the S–N data of the specimens tested at different frequencies, in which the lines denote the regression results of the fatigue life with the local stress amplitude in log-log scale. The experimental results of the specimens at the frequencies $f = 0.4$ Hz and 4 Hz are listed in Table 3. It is seen from Fig. 8 that the frequency has important influence on fatigue life. At the same stress amplitude, the fatigue life increases with increasing the frequency. It might be due to that the dislocations have more time to overcome obstacles under the lower frequency than the higher one [20], which increase the local plastic strain accumulation and lead to the shorter fatigue life under the lower frequency. This indicates that it is dangerous for evaluating the fatigue performance of structural components under very low frequency by the fatigue data test at the frequency of ~10 Hz. The results in Fig. 8 also indicate that the scatter of the fatigue life is related to both the stress amplitude and loading frequency. At low stress amplitudes, the scatter of the fatigue life tested at the frequency $f = 35$ Hz is larger than that tested at the frequencies $f = 0.4$ Hz and 4 Hz.

Fig. 9 shows the variation of the fatigue life with the frequency at the relative higher stress amplitude under which the scatter of the fatigue life is small for all the tested frequencies $f = 0.4$ Hz, 4 Hz and 35 Hz. The results are also compared with those of the same titanium alloy tested at a higher maximum stress (0.95 of the yield stress, $R = -1$) and much lower frequency under the conventional fatigue test with triangular wave form in literature [26]. It is seen that, similar to result for the effect of frequency on fatigue life observed in literature [26], the fatigue life and the frequency at the same stress amplitude could be well correlated by a linear relation in log-log scale, i.e.

$$\lg N_f = 0.1395 \times \lg f + 3.7333 \text{ for } \sigma_a = 882 \text{ MPa} \quad (7)$$

$$\lg N_f = 0.1995 \times \lg f + 3.971 \text{ for } \sigma_a = 819 \text{ MPa} \quad (8)$$

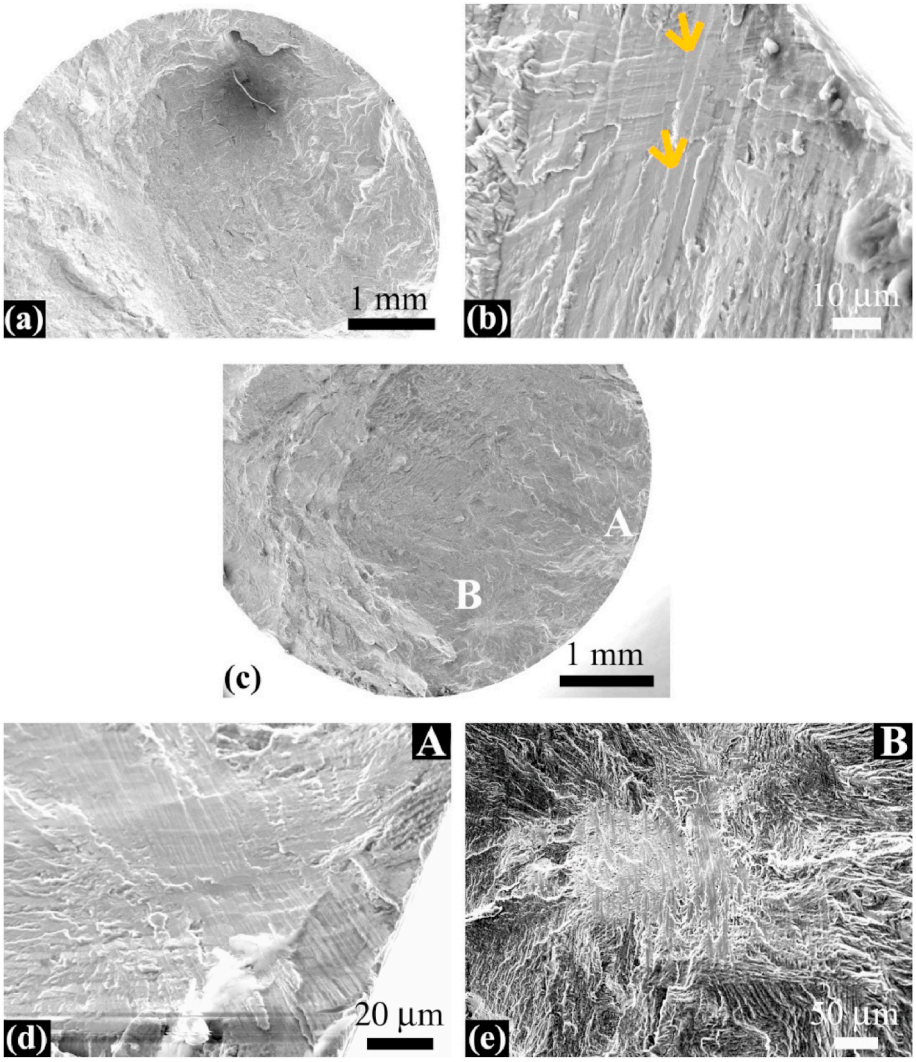

Fig. 6. Fracture surface morphology of failed specimens at the stress ratio $R = 0.1$. (a) and (b): Single crack initiation at $\sigma_{max} = 819$ MPa and $N_f = 5.66 \times 10^5$; (c)–(e): Multiple crack initiation at $\sigma_{max} = 882$ MPa and $N_f = 5.26 \times 10^5$. (a) and (c): Low magnification image of the fracture surface; (b) Close-up of crack initiation region in (a); (d) and (e) Close-ups of crack initiation regions at A and B in (c), respectively. The arrows in (b) point to the regions exhibiting the facet feature.

$$\lg N_f = 0.233 \times \lg f + 4.2693 \quad \text{for } \sigma_a = 756 \text{ MPa} \tag{9}$$

The correlation coefficients are 0.88, 0.92 and 0.83 for Eqs. (7)–(9), respectively, indicating that the correlation is highly significant for the fatigue life and the frequency in log-log scale [27]. Eqs. (7)–(9) also indicate that the slope of the fatigue life with the frequency in log-log scale tends to increase with decreasing the stress amplitude (the slope is 0.0986 for the fatigue life and the frequency in log-log scale at the stress amplitude 929.1 MPa [26]), i.e. the effect of frequency on fatigue life seems to be related to the stress amplitude, which is a little higher for the relative lower stress amplitude.

3.2.2. Fracture surface observation

The specimens tested at the frequencies $f = 0.4$ Hz and 4 Hz all fail from the specimen surface and some specimens present multiple crack initiation sites, as shown in Figs. 10 and 11. The facet feature is also observed in the crack initiation region of a few specimens at the frequencies $f = 0.4$ Hz and 4 Hz (Fig. 10d and e, Fig. 11b and e), similar to that at the frequency $f = 35$ Hz and $R = -1$. While for the specimens tested at the frequency $f = 35$ Hz and $R = -1$, no multiple crack initiation sites are observed in the fracture surface. The percentage of specimens with multiple crack initiation modes to the total specimens is 0, 42% and 54% at the frequencies $f = 35$ Hz, 4 Hz and 0.4 Hz, respectively. This indicates that the frequecny has influence on the crack initiation mode and the specimens at lower frequencies tend to fail with multiple crack initiation mode.

3.3. Crack initiation mechanism

SEM observation indicates that the fracture surfaces of the present titanium alloy exhibit two different characteristics in the crack initiation region. One is with facet feature and the other presents no facet feature. In order to understand the mechanism of the crack initiation especially the facet formation, the microstructure characteristic in the crack initiation region along with the spatial orientation and the crystallographic orientation of the facets are observed for the cross-section samples parallel to the loading direction.

Figs. 12 and 13 show the SEM and EBSD observations of the cross-section sample parallel to the loading direction in the crack initiation region with facet feature in Figs. 4d and 5e, respectively. Fig. 14 shows the SEM and EBSD results for the cross-section sample parallel to the loading direction at the crack initiation region without facet feature in

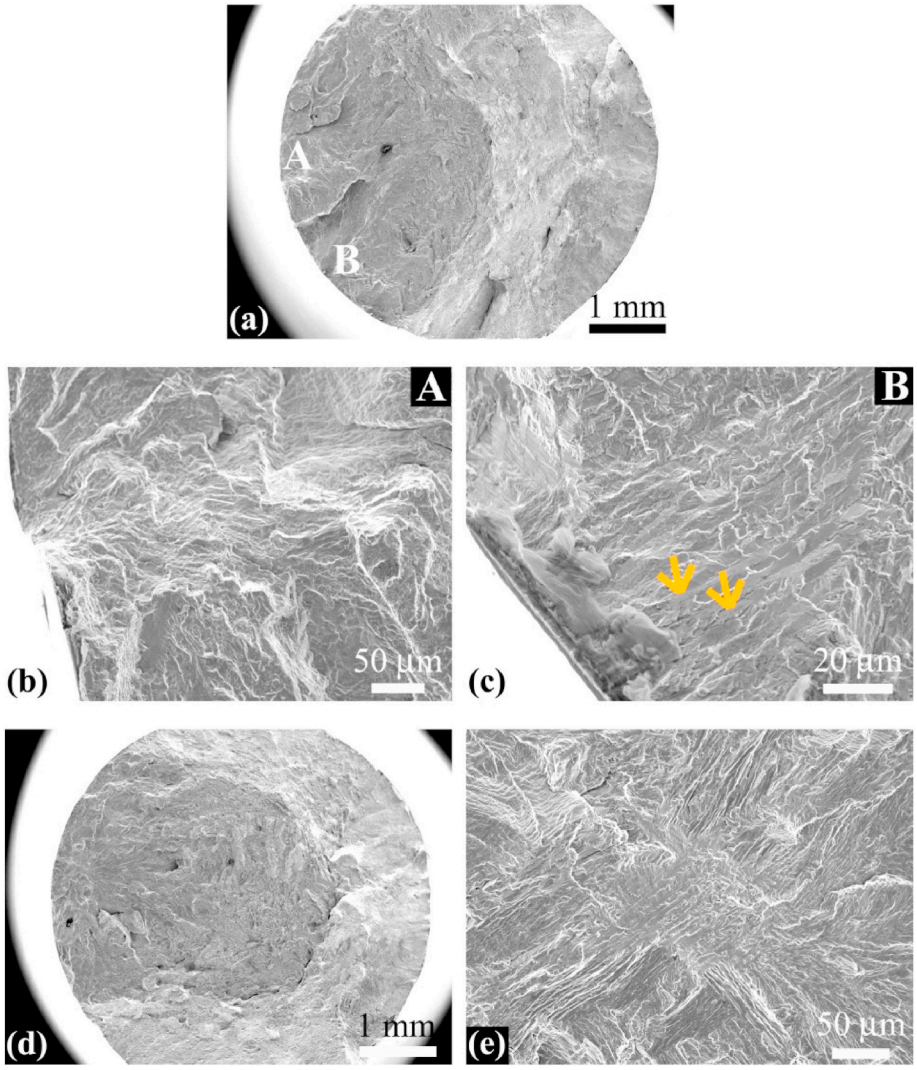

Fig. 7. Fracture surface morphology of failed specimens at the stress ratio $R = 0.3$. (a)–(c): Multiple crack initiation at $\sigma_{max} = 976.5$ MPa and $N_f = 4.37 \times 10^5$; (d) and (e): Single crack initiation at $\sigma_{max} = 976.5$ MPa and $N_f = 3.07 \times 10^5$. (a) and (d): Low magnification image of the fracture surface; (b) and (c) Close-ups of crack initiation regions at A and B in (a), respectively; (e) Close-up of crack initiation region in (d). The arrows in (c) point to the regions exhibiting the facet feature.

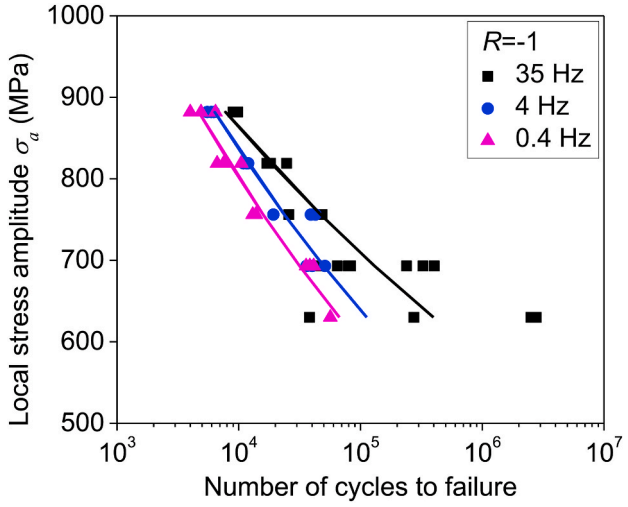

Fig. 8. S–N data of specimens at different frequencies, in which the lines denote the linear regression results of the fatigue life with the local stress amplitude in log-log scale.

Fig. 4b. It is seen that α phase lamellas responsible for the facets in Figs. 12 and 13 are both in relatively regular arrangement and the α grains are generally in similar crystallographic orientation. However, for the crack initiation region exhibiting a relative big facet region in Fig. 4d, it consists not only α phase lamella but also the β_{trans}, indicating that α grains are not the only phases responsible for the facets. While for the case of fracture surface exhibiting no facet feature in the crack initiation region in Fig. 14, the crack surface due to α grains are not flat and the α grains responsible for the crack surface are not in regular arrangement.

Further, by the consideration that the facet plane normal is almost parallel to the *x*-*y* plane in Figs. 12b and 13b after the normal direction of the polished surface of the cross-section sample rotates a small angle (about 5°) around the negative direction of *x* axis, the angle of the facet plane normal for the α grain with respect to the loading direction is approximately obtained by the angle of the intersecting line of the polished α grain and the crack surface with respect to *x* axis in Figs. 12b and 13b, respectively. The angles of the facet plane normal for the α grains numbered 1, 2 and 3 in Fig. 12c with respect to the loading direction are obtained as 38°, 34° and 34°, respectively. The angles of the facet plane normal for the α grains numbered 1, 2 and 3 in Fig. 13c with respect to the loading direction are obtained as 41°, 39° and 40°, respectively. This indicates that the facet plane is in high shear stress in

Table 3
Experimental results of specimens at frequencies $f = 0.4$ Hz and 4 Hz shown in Fig. 8.

$R = -1, f = 4$ Hz				$R = -1, f = 0.4$ Hz			
σ_a (MPa)	N_f	Origin location	Single or Multi-site	σ_a (MPa)	N_f	Origin location	Single or Multi-site
882	5.95×10^3	Surface	Single	882	4.90×10^3	Surface	Multi
882	5.52×10^3	Surface	Single	882	6.44×10^3	Surface	Multi
882	6.25×10^3	Surface	Multi	882	4.0×10^3	Surface	Single
819	1.09×10^4	Surface	Multi	819	1.05×10^4	Surface	Single
819	1.16×10^4	Surface	Multi	819	7.52×10^3	Surface	Multi
819	1.20×10^4	Surface	Multi	819	6.65×10^3	Surface	Multi
756	1.93×10^4	Surface	Single	756	1.38×10^4	Surface	Multi
756	3.91×10^4	Surface	Single	756	1.38×10^4	Surface	Multi
756	4.27×10^4	Surface	Single	756	1.30×10^4	Surface	Multi
693	4.01×10^4	Surface	Single	693	4.13×10^4	Surface	Single
693	5.11×10^4	Surface	Single	693	3.84×10^4	Surface	Single
693	3.60×10^4	Surface	Multi	693	3.58×10^4	Surface	Single
				630	5.65×10^4	Surface	Single

the spatial orientation.

It has been shown that the facets for titanium alloys could be formed by slip on basal planes or prismatic planes of α grains [24,25,28]. The results of the spatial orientation of facet planes and the crystallographic orientation of α grains responsible for facets in Figs. 12 and 13 indicate that the facets are not formed on basal planes or prismatic planes, i.e. the facet formation is not attributed to the basal slip or prismatic slip of α grains for the present titanium alloy. So, it is thought that, for the case of fracture surface exhibiting the facet feature in the crack initiation region, the facets are due to the cleavage of α grains by dislocation pile-ups at grain boundaries or high local stress field [25,29,30]. For the case of fracture surface exhibiting no facet feature in the crack initiation region, Fig. 14b indicates that the cracks nucleate and initiate at α grains or interfaces due to the microstructure inhomogeneity and deformation incompatibility [31].

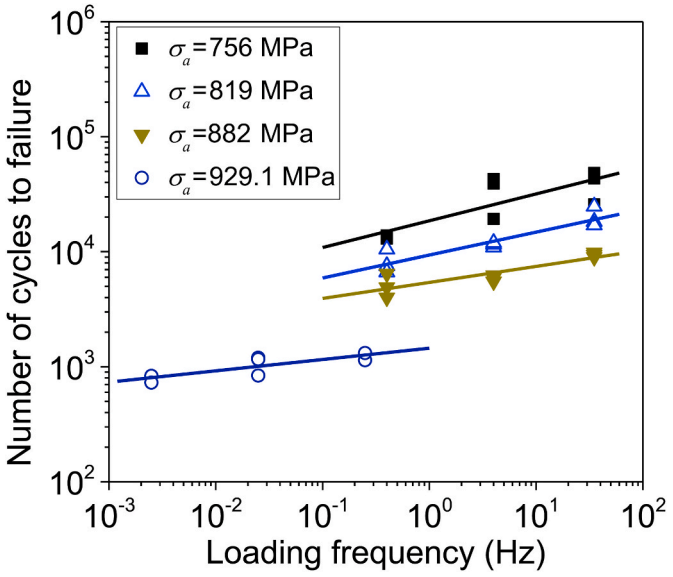

Fig. 9. Variation of fatigue life with loading frequency, in which the lines denote the linear regression results of the fatigue life with the frequency in log-log scale.

4. Conclusions

In this paper, we investigate the effects of stress ratio and loading frequency on the fatigue behavior of the titanium alloy Ti–6Al–2Sn–2Zr–3Mo-X with basketweave microstructure by axial loading fatigue test. Cross-section samples parallel to the loading direction in crack initiation regions are prepared by FIB technique and then observed by SEM and EBSD. The main results are as follows.

(1) SEM observation indicates that the fracture surfaces present two different characteristics in the crack initiation region at all the tested stress ratios $R = -1$, -0.5, 0.1 and 0.3. One has facet feature and the other has no facet feature. SEM and EBSD observations indicate that the facets in the crack initiation region are due to the cleavage of α grains at high shear stress in the spatial orientation.

(2) At the frequency $f = 35$ Hz, both the single and multiple crack initiation modes are observed at the stress ratios $R = -0.5$, 0.1 and 0.3, while only single crack initiation mode presents at $R = -1$. The relative higher stress ratio seems to have higher probability for the occurrence of multiple crack initiation mode. The stress ratio has substantial influence on fatigue life. The fatigue life N_f, stress amplitude $\sigma_{a,R}$ and stress ratio R could be expressed as $N_f = A\ [(1–R)/2]^l \sigma^m{}_{a,R}$, where A, l and m are material parameters.

(3) The loading frequecny ($f = 0.4$ Hz, 4 Hz and 35 Hz) has influence on the crack initiation mode. The specimens at lower frequencies ($f = 0.4$ Hz and 4 Hz) tend to fail with multiple crack initiation mode. Moreover, it has important influence on fatigue life, and the scatter of the fatigue life depends on both the stress amplitude and the loading frequency. At relative higher stress amplitude, the fatigue life and the frequency could be correlated by a linear relation in log-log scale.

(4) The paper indicates that the present titanium alloy Ti–6Al–2Sn–2Zr–3Mo-X exhibits two different crack initiation mechanism. One is due to the cleavage of α grains by dislocation pile-ups at grain boundaries or high local stress field. For this case, the crack initiates following the cleavage of α grains and the fracture surface exhibits facet feature in the crack initiation region. The other is due to the microstructure inhomogeneity and deformation incompatibility of different phases. For this case, the crack initiates at α grains or interfaces and the fracture surface presents no facet feature in the crack initiation region.

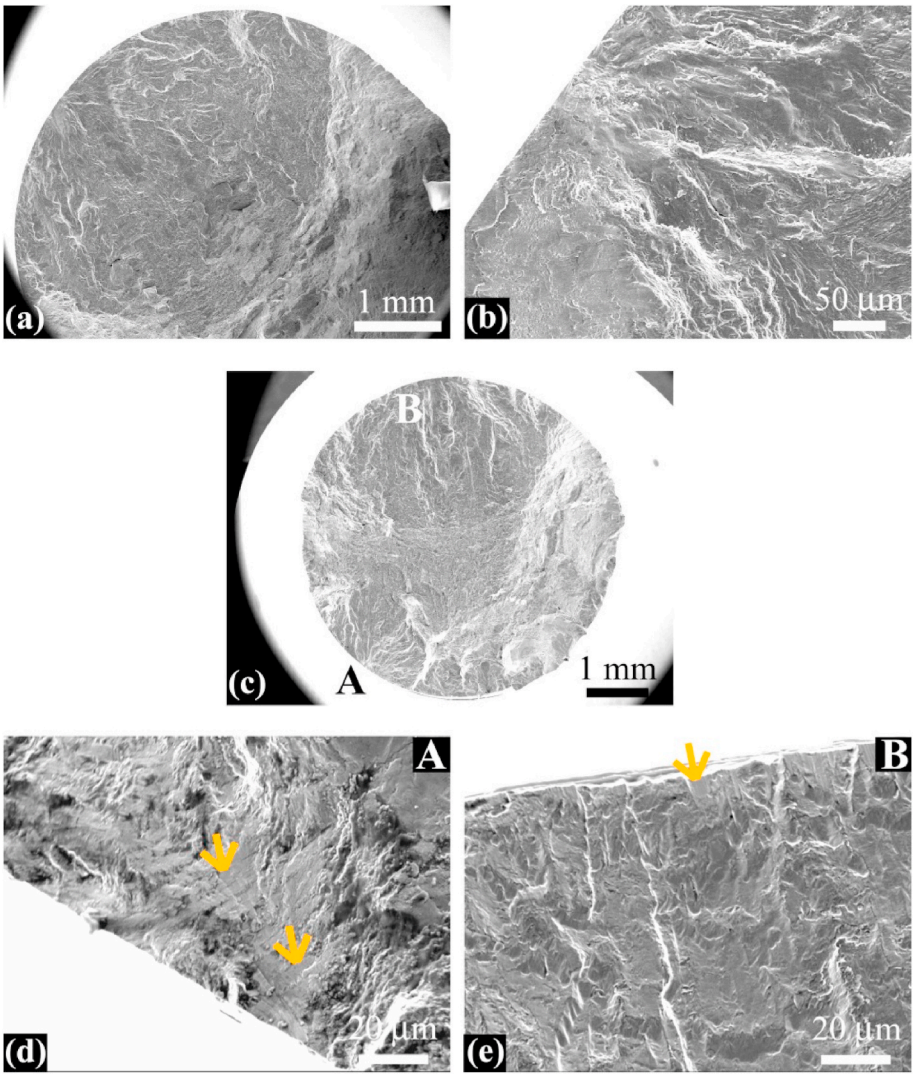

Fig. 10. Fracture surface morphology of failed specimens at the frequency $f = 4$ Hz and stress ratio $R = -1$. (a) and (b): Single crack initiation at $\sigma_a = 756$ MPa and $N_f = 1.93 \times 10^4$; (c)–(e): Multiple crack initiation at $\sigma_a = 819$ MPa and $N_f = 1.2 \times 10^4$. (a) and (c): Low magnification image of the fracture surface; (b) Close-up of crack initiation region in (a); (d) and (e) Close-ups of crack initiation regions at A and B in (c), respectively. The arrows in (d) and (e) point to the regions exhibiting the facet feature.

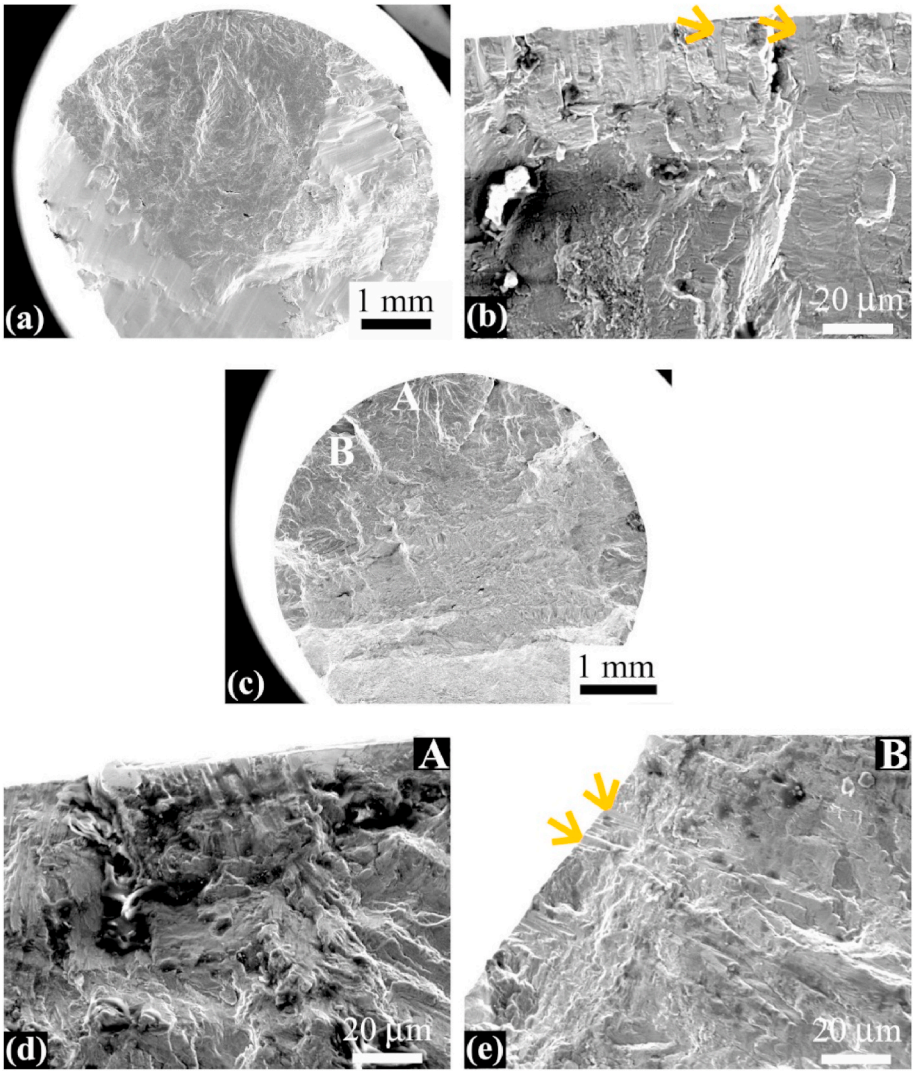

Fig. 11. Fracture surface morphology of failed specimens at the frequency $f = 0.4$ Hz and stress ratio $R = -1$. (a) and (b): Single crack initiation at $\sigma_a = 819$ MPa and $N_f = 1.05 \times 10^4$; (c)–(e): Multiple crack initiation at $\sigma_a = 882$ MPa and $N_f = 6.44 \times 10^3$. (a) and (c): Low magnification image of the fracture surface; (b) Close-up of crack initiation region in (a); (d) and (e) Close-ups of crack initiation regions at A and B in (c), respectively. The arrows in (b) and (e) point to the regions exhibiting the facet feature.

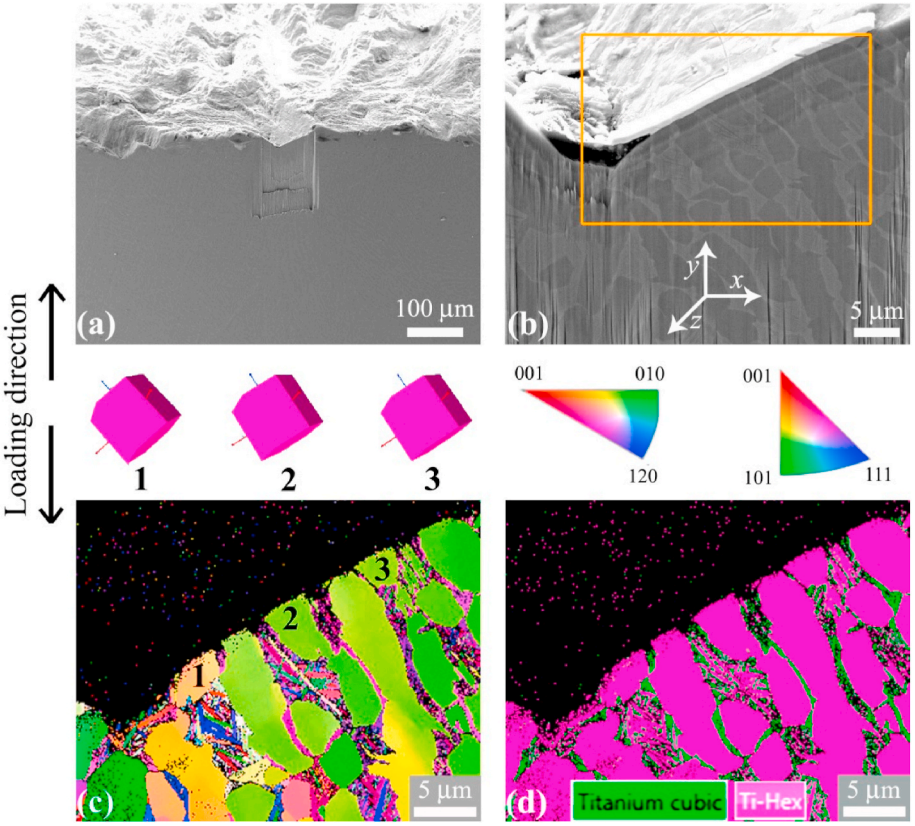

Fig. 12. SEM and EBSD results for the cross-section sample parallel to the loading direction at the crack initiation region in Fig. 4d. (a): SEM image of the cross-section sample observed perpendicular to the polished surface of the cross-section sample; (b): Close-up of the cross-section sample in (a), in which the *x*-*y* plane in the coordinate system is set to be perpendicular to the observation direction and the rectangle denotes the region for EBSD observation; (c) and (d): EBSD inverse pole figure map and phase map for the rectangle region in (b), in which the hexagonal unit denotes the crystal orientation of the numbered α grains.

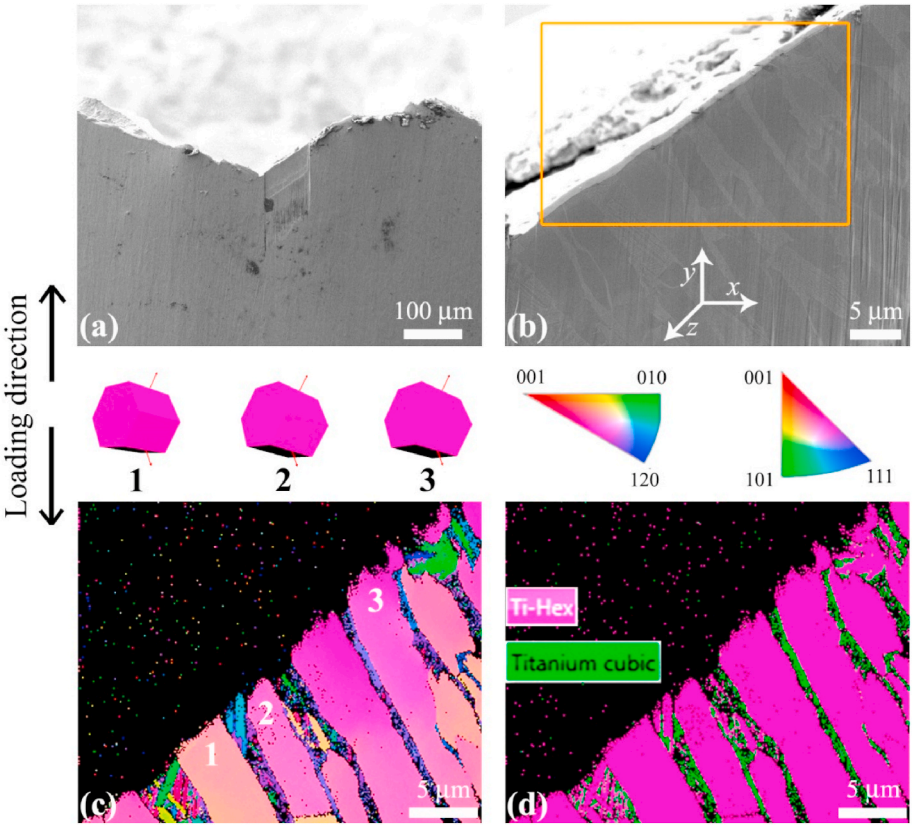

Fig. 13. SEM and EBSD results for the cross-section sample parallel to the loading direction at the crack initiation region in Fig. 5e. (a): SEM image of the cross-section sample observed perpendicular to the polished surface of the cross-section sample; (b): Close-up of the cross-section sample in (a), in which the *x*-*y* plane in the coordinate system is set to be perpendicular to the observation direction and the rectangle denotes the region for EBSD observation; (c) and (d): EBSD inverse pole figure map and phase map for the rectangle region in (b), in which the hexagonal unit denotes the crystal orientation of the numbered α grains.

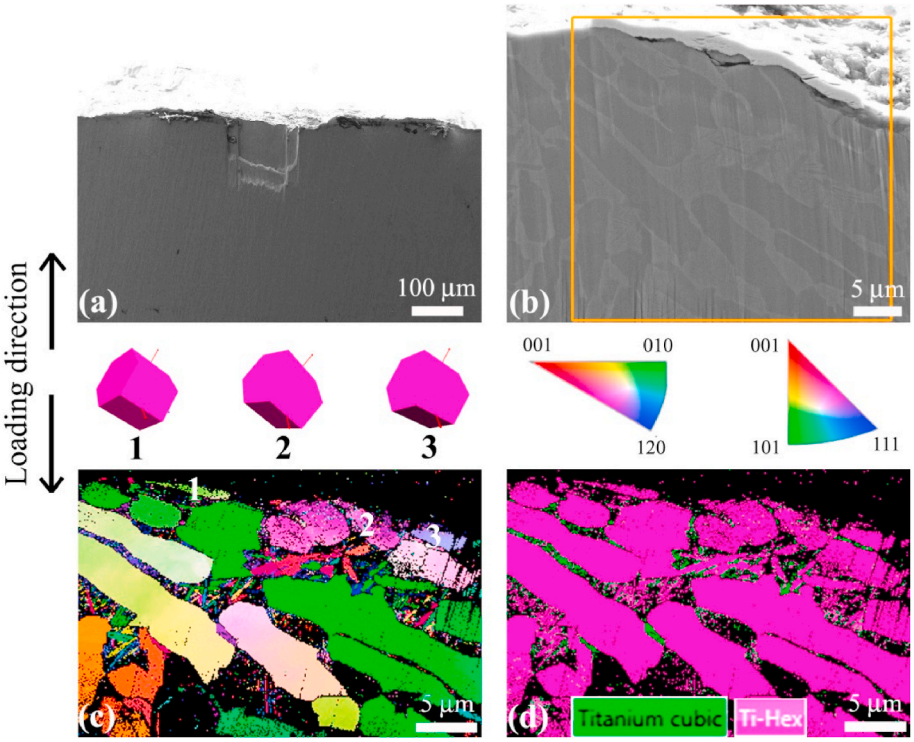

Fig. 14. SEM and EBSD results for the cross-section sample parallel to the loading direction at the crack initiation region in Fig. 4b. (a): SEM image of the cross-section sample observed perpendicular to the polished surface of the cross-section sample; (b): Close-up of the cross-section sample in (a), in which the rectangle denotes the region for EBSD observation; (c) and (d): EBSD inverse pole figure map and phase map for the rectangle region in (b), in which the hexagonal unit denotes the crystal orientation of the numbered α grains.

The present results are helpful for understanding the effects of stress ratio and loading frequency on the crack initiation mechanism and fatigue life of titanium alloys.

Data availability

The data are available upon request by contacting with the corresponding author.

CRediT authorship contribution statement

Chengqi Sun: Conceptualization, Methodology, Formal analysis, Investigation, Writing - original draft, Writing - review & editing, Supervision. **Yanqing Li:** Formal analysis, Writing - review & editing. **Ruxu Huang:** Formal analysis, Writing - review & editing. **Lei Wang:** Formal analysis, Writing - review & editing. **Jialong Liu:** Formal analysis. **Lingling Zhou:** Writing - review & editing. **Guihua Duan:** Writing - review & editing.

Declaration of competing interest

The authors declare that they have no known competing financial interests or personal relationships that could have appeared to influence the work reported in this paper.

Acknowledgements

The authors gratefully acknowledge the support of the National Key Research and Development Program of China (2017YFC0305500).

References

[1] G.K. Haritos, T. Nicholas, D.B. Lanning, Notch size effects in HCF behavior of Ti-6Al-4V, Int. J. Fatig. 21 (1999) 643–652.
[2] W. Xu, X. Yang, B. Zhong, G. Guo, L. Liu, C. Tao, Multiaxial fatigue investigation of titanium alloy annular discs by a vibration-based fatigue test, Int. J. Fatig. 95 (2017) 29–37.
[3] W. Xu, X. Yang, B. Zhong, Y. He, C. Tao, Failure criterion of titanium alloy irregular sheet specimens for vibration-based bending fatigue testing, Eng. Fract. Mech. 195 (2018) 44–56.
[4] B. Nie, Z. Zhao, Y. Ouyang, D. Chen, H. Chen, H. Sun, S. Liu, Effect of low cycle fatigue predamage on very high cycle fatigue behavior of TC21 titanium alloy, Materials 10 (2017) 1384.
[5] F. Wang, W. Cui, Experimental investigation on dwell-fatigue property of Ti-6Al-4V ELI used in deep-sea manned cabin, Mater. Sci. Eng., A 642 (2015) 136–141.
[6] C. Sun, Q. Song, A method for evaluating the effects of specimen geometry and loading condition on fatigue life of metallic materials, Mater. Res. Express 6 (2019), 046536.
[7] Y. Furuya, E. Takeuchi, Gigacycle fatigue properties of Ti–6Al–4V alloy under tensile mean stress, Mater. Sci. Eng., A 598 (2014) 135–140.
[8] W. Li, H. Zhao, A. Nehila, Z. Zhang, T. Sakai, Very high cycle fatigue of TC4 titanium alloy under variable stress ratio: failure mechanism and life prediction, Int. J. Fatig. 104 (2017) 342–354.
[9] Y. Ono, T. Yuri, T. Ogata, S. Matsuoka, H. Sunakawa, Effect of stress ratio on high-cycle fatigue properties of Ti-6Al-4V ELI alloy forging at low temperature, AIP Conf. Proc. 1574 (2014) 23–26.
[10] R.K. Nalla, B.L. Boyce, J.P. Campbell, J.O. Peters, R.O. Ritchie, Influence of microstructure on high-cycle fatigue of Ti-6Al-4V: bimodal vs. lamellar structures, Metall. Mater. Trans. A 33 (2002) 899–918.
[11] Y. Li, Q. Song, S. Feng, C. Sun, Effects of loading frequency and specimen geometry on high cycle and very high cycle fatigue life of a high strength titanium alloy, Materials 11 (2018) 1628.
[12] K. Tokaji, H. Kariya, Mean stress dependence of fatigue strength and subsurface crack initiation in Ti–15Mo–5Zr–3Al alloy, Mater. Sci. Eng., A 281 (2000) 268–274.
[13] J. Lindemann, L. Wagner, Mean stress sensitivity in fatigue of α, (α+β) and β titanium alloys, Mater. Sci. Eng., A 234-236 (1997) 1118–1121.
[14] X. Liu, C. Sun, Y. Hong, Effects of stress ratio on high-cycle and very-high-cycle fatigue behavior of a Ti–6Al–4V alloy, Mater. Sci. Eng., A 622 (2015) 228–235.
[15] L.E. Matokhnyuk, A.V. Voinalovich, A.A. Khlyapov, S.G. Bulgakova, V. P. Artyushina, Fatigue limit of the titanium alloy VT23 in tests with high loading frequency, Met. Sci. Heat Treat 30 (1988) 786–789.
[16] A.Y. Krasovskii, Y.N. Petrov, G.N. Nadezhdin, L.E. Matokhnyuk, V.L. Svechnikov, T.Y. Yakovleva, Fatigue damage to a pseudo-α-titanium alloy in the 10–33-Hz frequency range, Strength Mater. 14 (1982) 1320–1323.
[17] R.J. Morrissey, T. Nicholas, Staircase testing of a titanium alloy in the gigacycle regime, Int. J. Fatig. 28 (2006) 1577–1582.
[18] Z.Y. Huang, H.Q. Liu, H.M. Wang, D. Wagner, M.K. Khan, Q.Y. Wang, Effect of stress ratio on VHCF behavior for a compressor blade titanium alloy, Int. J. Fatig. 93 (2016) 232–237.

[19] E. Takeuchi, Y. Furuya, N. Nagashima, S. Matsuoka, The effect of frequency on the giga-cycle fatigue properties of a Ti-6Al-4V alloy, Fatig. Fract. Eng. Mater. Struct. 31 (2008) 599–605.
[20] R.J. Morrissey, D.L. McDowell, Frequency and stress ratio effects in high cycle fatigue of Ti-6Al-4V, Int. J. Fatig. 21 (1999) 679–685.
[21] Y. Murakami, T. Nomoto, T. Ueda, Factors influencing the mechanism of superlong fatigue failure in steels, Fatig. Fract. Eng. Mater. Struct. 22 (1999) 581–590.
[22] C. Sun, Z. Lei, Y. Hong, Effects of stress ratio on crack growth rate and fatigue strength for high cycle and very-high-cycle fatigue of metallic materials, Mech. Mater. 69 (2014) 227–236.
[23] C. Sun, X. Zhang, X. Liu, Y. Hong, Effects of specimen size on fatigue life of metallic materials in high-cycle and very-high-cycle fatigue regimes, Fatig. Fract. Eng. Mater. Struct. 39 (2016) 770–779.
[24] C.J. Szczepanski, S.K. Jha, J.M. Larsen, J.W. Jones, Microstructural influences on very high cycle fatigue crack initiation in Ti-6246, Metall. Mater. Trans. A 39 (2008) 2841–2851.
[25] J. Everaerts, B. Verlinden, M. Wevers, Investigation of fatigue crack initiation facets in Ti-6Al-4V using focused ion beam milling and electron backscatter diffraction, J Microsc-Oxford 267 (2017) 57–69.
[26] Q. Song, Y. Li, L. Wang, R. Huang, C. Sun, Effect of rise and fall time on dwell fatigue behavior of a high strength titanium alloy, Metals 9 (2019) 914.
[27] J.R. Taylor, An Introduction to Error Analysis, second ed., University Science Books, California, 1997.
[28] W.J. Evans, M.R. Bache, Dwell-sensitive fatigue under biaxial loads in the near-alpha titanium alloy IMI685, Int. J. Fatig. 16 (1994) 443–452.
[29] D.F. Neal, P.A. Blenkinsop, Internal fatigue origins in alpha-beta titanium-alloys, Acta Metall. 24 (1976) 59–63.
[30] R.J.H. Wanhill, A consideration of cleavage in alpha titanium, Acta Metall. 21 (1973) 1253–1258.
[31] J.H. Zuo, Z.G. Wang, E.H. Han, Effect of microstructure on ultra-high cycle fatigue behavior of Ti-6Al-4V, Mater. Sci. Eng., A 473 (2008) 147–152.